

This is the accepted manuscript made available via CHORUS. The article has been published as:

Insights into the atomic structure of the interface of ferroelectric $\text{Hf}_{0.5}\text{Zr}_{0.5}\text{O}_2$ grown epitaxially on $\text{La}_2\text{Mo}_3\text{SrMn}_3\text{O}_{13}$

$\text{Hf}_{0.5}\text{Zr}_{0.5}\text{O}_2$ grown epitaxially on $\text{La}_2\text{Mo}_3\text{SrMn}_3\text{O}_{13}$

Saúl Estandía, Tengfei Cao, Rohan Mishra, Ignasi Fina, Florencio Sánchez, and Jaume Gazquez

Phys. Rev. Materials **5**, 074410 — Published 28 July 2021

DOI: [10.1103/PhysRevMaterials.5.074410](https://doi.org/10.1103/PhysRevMaterials.5.074410)

Insights into the Atomic Structure of the Interface of Ferroelectric $\text{Hf}_{0.5}\text{Zr}_{0.5}\text{O}_2$ grown epitaxially on $\text{La}_{2/3}\text{Sr}_{1/3}\text{MnO}_3$

Saúl Estandía^{1,*†}, Tengfei Cao^{2,†}, Rohan Mishra^{2,*}, Ignasi Fina¹, Florencio Sánchez¹, and Jaume Gazquez¹

¹ *Institut de Ciència de Materials de Barcelona (ICMAB-CSIC), Campus UAB, Bellaterra, 08193 Barcelona, Spain*

² *Department of Mechanical Engineering & Materials Science, and Institute of Materials Science & Engineering, Washington University in St. Louis, One Brookings Drive, St. Louis, MO 63130, USA*

Epitaxial growth of $\text{Hf}_{0.5}\text{Zr}_{0.5}\text{O}_2$ (HZO) thin films allows for the stabilization of the metastable orthorhombic phase with robust ferroelectric properties. So far, the ferroelectric phase is most commonly stabilized on perovskite substrates upon insertion of a buffer layer of $\text{La}_{2/3}\text{Sr}_{1/3}\text{MnO}_3$ (LSMO); however, little is known about the role played by the LSMO buffer layer and the interface between HZO and LSMO. Inspection of a HZO/LSMO/ SrTiO_3 heterostructure, by scanning transmission electron microscope imaging and electron energy loss spectroscopy shows that despite the substantial structural mismatch between HZO and LSMO, the interface between them is relatively sharp spanning ~ 2 atomic layers. The LSMO surface, expected to be mostly MnO_2 -terminated, undergoes a chemical reconstruction consisting in the substitution of the Mn cations by a mixture of Hf/Zr cations. Density-functional-theory calculations show that the substitution of Mn by Hf on the MnO_2 -terminated surface of LSMO is energetically favorable, as the higher electronegativity and valence of Hf with respect to Mn balances the surface charge of the MnO_2 layer.

I. INTRODUCTION

Ferroelectric HfO_2 -based materials are promising because they are highly compatible with CMOS fabrication processes, and they exhibit ferroelectricity even at a thickness of only a few unit cells, at which most ferroelectrics become depolarized. [1–3] Since the discovery of ferroelectricity in a metastable phase of Si-doped HfO_2 , [4] numerous advances have been made with HfO_2 -based materials; for example, tunnel junctions [5–7] and ferroelectric random-access

memories [8,9] have been fabricated. HfO_2 -based materials are generally prepared as polycrystalline films; [10] and the metastable ferroelectric phase is stabilized by introducing different dopants or by alloying with other cations. [11,12] Among these variants, $\text{Hf}_{0.5}\text{Zr}_{0.5}\text{O}_2$ (HZO) has shown especially robust ferroelectric properties. [13] Beyond polycrystalline films, epitaxial films can be particularly useful to controllably tune the ferroelectric properties of the films. Ferroelectric HfO_2 thin films with different dopants have been grown epitaxially on various substrates such as the fluorite yttria-stabilized zirconia (YSZ), [14–16] Si, [17] pyrochlore oxides [18] or perovskites like SrTiO_3 (STO), [19,20] LaAlO_3 [21] or GdScO_3 . [22] On the perovskite substrates, a strained $\text{La}_{2/3}\text{Sr}_{1/3}\text{MnO}_3$ (LSMO) buffer layer or a similar manganite buffer is generally essential to stabilize the

[†]These authors contributed equally to this work.

*Corresponding authors:

saul.estandia@gmail.com

rmishra@wustl.edu

metastable ferroelectric phase, [19–21,23] with Nb-doped STO being the only perovskite substrate reported to permit the stabilization of the orthorhombic phase without the use of manganite buffers, [24] as far as we know.

HZO and LSMO have dissimilar structures; the fluorite-like structure of HZO and the perovskite structure of LSMO have a large lattice mismatch and different symmetry. Yet, HZO is epitaxially stabilized in several phases and orientations when deposited on LSMO. The ferroelectric phase of HZO (o-HZO) is generally attributed to the orthorhombic $Pca2_1$ structure, [25] and it seems that LSMO is crucial to stabilize it. For instance, by excluding the LSMO buffer layer, Lyu et al. reported that the growth of HZO on a $LaNiO_3$ electrode did not yield ferroelectric o-HZO, [17] even though the lattice parameters of $LaNiO_3$ are close to those of LSMO (only 0.5% mismatch). The HZO/LSMO heterointerface studied here, grown on STO, yields o-HZO with (111) orientation, in coexistence with the non-ferroelectric monoclinic phase, as has been reported previously. [6,22,26] Domain matching epitaxy has been proposed to explain the stabilization of o-HZO on LSMO electrodes, [26] as well as interface reconstructions leading to the formation of a metastable tetragonal phase at the interface. [19] However, the precise atomic structure of the HZO/LSMO heterointerface remains unknown.

Here, we provide insights into the structure and chemistry of the HZO/LSMO interface in a HZO/LSMO/STO heterostructure. By combining scanning transmission electron microscopy (STEM) and density-functional-theory (DFT) calculations, we reveal that the epitaxial heterointerface is mediated by a coherent interfacial monolayer between the HZO and LSMO structures. This monolayer is formed through a chemical reconstruction of the LSMO termination surface, consisting of the substitution of the Mn of the uppermost MnO_2 layer of the LSMO [27,28] by a mixture of Hf and Zr. Z-contrast imaging and electron energy loss (EEL) spectroscopy reveal a lower concentration of Hf/Zr in the first HZO plane and the presence of oxygen vacancies at the interface. DFT calculations indicate that the substitution of Mn on the MnO_2 -terminated surface of

LSMO with Hf, together with oxygen vacancies, contributes to surface charge balance, and is energetically favorable, which explains the STEM observations. The nature of the heterointerface that enables the epitaxial growth of ferroelectric o-HZO films grown on perovskites is thus revealed.

II. EXPERIMENTAL SECTION

Thin films deposition: an epitaxial heterostructure formed by HZO (top layer, $t = 10$ nm) and LSMO (bottom layer, $t = 25$ nm) was grown on $SrTiO_3(001)$. The HZO/LSMO heterostructure was deposited in a single process by pulsed laser deposition (KrF excimer laser). Detailed information on growth conditions and ferroelectric properties is reported elsewhere. [20,22]

Ferroelectric characterization: the capacitor measuring configuration was obtained by ex situ deposition through stencil masks of top platinum electrodes, 20 nm in thickness and 19 μm in diameter, by dc magnetron sputtering. The ferroelectric polarization loop was obtained at room temperature in top-bottom configuration by means of an AixACCT TFAAnalyser2000 platform with a pulse frequency of 1 kHz. Leakage contribution was compensated using a dynamic leakage current compensation standard procedure. [29,30]

Structural characterization: for the characterization of the HZO interface, STEM images and electron energy loss spectra were acquired with an aberration corrected Nion UltraSTEM 200, operated at 200 kV and equipped with a 5th order Nion aberration corrector and with a Gatan Enfium spectrometer. For high-angle annular dark field (HAADF) Z-contrast imaging a probe convergence angle of 30 mrad and an annular dark-field detector with an inner angle greater than 86 mrad were used. For EELS, the collection semi-angle was 48 mrad. HAADF images of cross-sectional specimens were recorded as-viewed along [100] and [110] zone axes of the substrate. The TEM specimens were prepared by the conventional method of cutting-gluing-slicing-polishing (mechanical + ion milling). Regarding the

EELS characterization, a 62×160 pixels spectrum image (containing a spectrum for each pixel or probe position) was acquired with an exposure time of 0.1 s per pixel, simultaneously with the HAADF image. Then, the chemical maps were obtained after removal of the background, which was fitted to an exponential decay law, and further integration of the intensity within a window starting at the edge energy. This is done for each pixel in the spectrum image. EEL spectrum images were typically acquired from relatively thin regions, with thickness values in terms of the inelastic mean free path $t/\lambda < 0.5$, and were acquired with an energy dispersion of 1 eV/channel for compositional maps and 0.3 eV/channel for the study of the electronic fine structure.

Computational details: we have used density-functional-theory (DFT) calculations to investigate the likelihood of Hf adatoms to substitute Mn atoms at MnO₂-terminated surface of LSMO. We have optimized all our structures using DFT as implemented in the VASP package. [31] The energy cutoff for the plane waves was set at 500 eV. The threshold for energy convergence for the self-consistent loop was set to 1e-6 eV, and the convergence criterion for forces was set to 0.01 eV Å⁻¹. We used projector augmented-wave (PAW) potentials [32] and the generalized gradient approximation (GGA) within the Perdew-Burke-Ernzerhof (PBE) parameterization [33] to describe the electron-ion and the electronic exchange-correlation interactions. We used orthogonal slabs of (001)-oriented La_{0.75}Sr_{0.25}MnO₃ having symmetric MnO₂ termination at both the surfaces. The in-plane dimensions of the slab were 2×2 times that of a 5-atom perovskite unit-cell. The thickness of the slab was 3.5 unit cells. The atoms in the central layer are fixed to their bulk coordinates. We used a vacuum of 30 Å to minimize interactions between the slab and its periodic images. The Brillouin zone was sampled by a $4 \times 4 \times 1$ k -points mesh obtained using the Monkhorst-Pack scheme. [34] We imposed ferromagnetic ordering of Mn atoms, which is the ground state for La_{0.75}Sr_{0.25}MnO₃ and the experimentally used La_{0.66}Sr_{0.33}MnO₃ composition. [35] We imposed the $a^-b^-c^+$ tilting

pattern under the Glazer's notation for the MnO₆ octahedral network. [36] Bader charge of each atom in the terminated layer and valence electrons of each element are applied to analyze surface charge states. For example, for the terminated MnO₂ surface, the average bader charge of Mn and O are 5.4 e and 7.2 e (Table I), respectively. For Mn and O elements, their valence electrons are 7 e and 6 e. Therefore, the charge of each MnO₂ unit is $(7-5.4) e + (6-7.08) * 2 e = 0.52 e$. There are four MnO₂ units in terminated layer, and the total surface charge is 2.08 e. To compare the stability of different HfO_x adsorbates on MnO₂-terminated LSMO under different growth conditions, we have calculated the adsorbate energy, $\sigma(\text{HfO}_x)$, as a function of the chemical potentials of Hf and O, μ_{Hf} and μ_{O} , respectively, using Eq. 1:

$$\sigma(\text{HfO}_x) = E_{slab}(\text{HfO}_x/\text{LSMO}) - E_{slab}(\text{LSMO}) + \mu_{\text{Hf}} + x\mu_{\text{O}} \quad (\text{Eq.1})$$

Here, $E_{slab}(\text{HfO}_x/\text{LSMO})$ is the DFT-calculated energy of HfO_x adsorbates, in their most stable configuration for each x , on MnO₂-terminated LSMO, and $E_{slab}(\text{LSMO})$ is the energy of the bare MnO₂-terminated LSMO slab. The chemical potentials can vary from Hf-rich (O-poor) conditions to Hf-poor (O-rich conditions). For the former, Hf is assumed to be in equilibrium with bulk Hf metal in hcp phase, while for the latter, oxygen is assumed to be in equilibrium with oxygen gas, which in our case is the DFT-energy of an isolated O₂ molecule in its triplet state. Specifically, μ_{Hf} and μ_{O} for the two conditions are defined as:

Hf-rich (O-poor) case:

$$\mu_{\text{Hf}} = E_{bulk}(\text{Hf}); \mu_{\text{O}} = \frac{1}{2}[E_{bulk}(\text{HfO}_2) - \mu_{\text{Hf}}] \quad (\text{Eq.2})$$

Hf-poor (O-poor) case:

$$\mu_{\text{O}} = \frac{1}{2}E(\text{O}_2); \mu_{\text{Hf}} = E_{bulk}(\text{HfO}_2) - 2\mu_{\text{O}} \quad (\text{Eq.3})$$

In the above, $E_{bulk}(\text{HfO}_2)$ is the energy of HfO₂ in its ground state (monoclinic phase). Using these, we find that under Hf-rich conditions, $\mu_{\text{Hf}} = -9.96$ eV and $\mu_{\text{O}} = -10.32$ eV; and under Hf-poor conditions, $\mu_{\text{Hf}} = -21.76$ eV and $\mu_{\text{O}} = -4.42$ eV.

Additionally, as the MnO₂-terminated LSMO slab is rich in Mn, we assume that it is in equilibrium with bulk Mn, which adds an additional bound on μ_{O} , as follows:

$$\mu_{\text{Mn}} = E_{\text{bulk}}(\text{Mn}); \mu_{\text{O}} = \frac{1}{2}[E_{\text{bulk}}(\text{MnO}_2) - \mu_{\text{Mn}}] \text{ (Eq. 4)}$$

where $E_{\text{bulk}}(\text{MnO}_2)$ is the energy of β -MnO₂. Based on this bound, we find that $-6.92 \text{ eV} \leq \mu_{\text{O}} \leq -4.42 \text{ eV}$.

III. RESULTS AND DISCUSSION

A HZO film was grown epitaxially on a (001)-oriented STO substrate buffered with LSMO. LSMO grows with a cube-on-cube orientation relationship on (001)-oriented STO. As reported elsewhere, [22] o-HZO (111)-oriented crystallites coexist with non-ferroelectric monoclinic (001)-oriented crystallites in the studied film, both phases being epitaxial to LSMO. Among different bottom electrodes, only LSMO stabilizes the o-HZO phase, while other perovskite electrodes, such as LaNiO₃ or SrRuO₃, only yield monoclinic HZO (m-HZO). [23] The ferroelectric character of the studied film is revealed by an I-V curve and the corresponding integrated P-V loop (see Figure S1, Supplemental Material [37]), with ferroelectric switching peaks at around 3-4V and remanent polarization of around 12 $\mu\text{C}/\text{cm}^2$. Further macroscopic ferroelectric characterization of this film has been reported elsewhere. [22,23] Herein, we focus on the interface between the ferroelectric o-HZO and the LSMO buffer layer, although the interface between the paraelectric monoclinic phase of HZO and the LSMO buffer was also studied in detail, revealing small differences with the orthorhombic phase (see Figures S2 and S3, Supplemental Material [37]).

Figure 1a and b show two high-angle annular dark field (HAADF or Z-contrast) images of the interface between (111) o-HZO and the LSMO layer viewed along the [100] and [110] LSMO zone axis, respectively; as a consequence, o-HZO is also viewed along two different zone axes. The (111) o-HZO crystallites are twinned on the four-fold LSMO surface, implying that o-HZO grains can grow along

either [0-22] or [-211] directions aligned with [110] of LSMO. [26] The o-HZO (111) grain in Figure 1a is not viewed along a major crystallographic direction. As a result, the Z-contrast image shows only bright stripes corresponding to the out-of-plane (111) cation planes of HZO. On the other hand, the crystal structure of [0-22] and [-211] HZO grains, shown in Figure 1b and 1c, respectively, become visible when the heterostructure is viewed along the substrate's [110] zone axis.

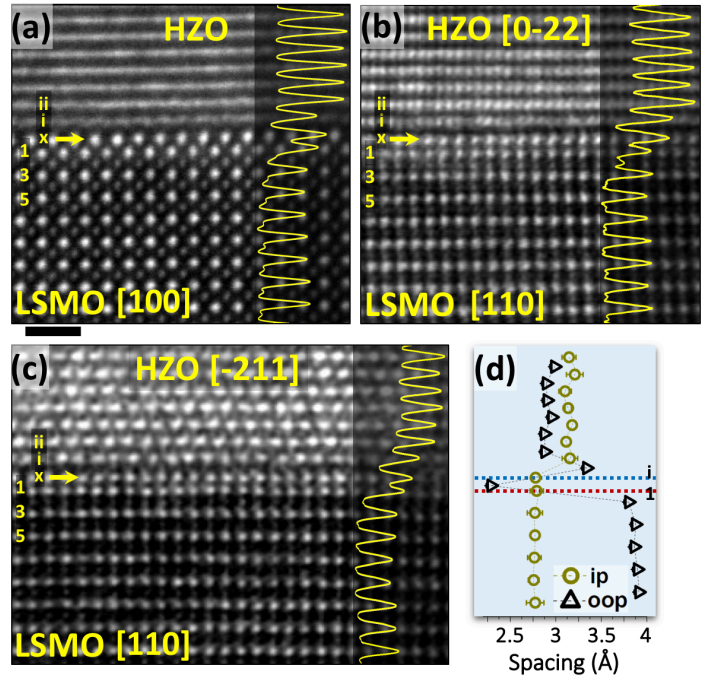


FIG. 1. (a) Z-contrast image of the HZO/LSMO interface along the [100] LSMO zone-axis. (b) and (c) show images along the [110] LSMO zone-axis, displaying the two possible zone axes (according to the in-plane HZO twins) for the o-HZO grains. No HZO zone axis is close to the substrate [100] zone-axis in (a), and as a result, the HZO atomic columns are visible as bright horizontal stripes. The interface monolayer is denoted as “x” and it is indicated by a yellow arrow in the three images, while the first atomic plane of the o-HZO layer is marked with an “i”. The row-averaged intensity profiles across the interface (along the out-of-plane direction) are shown on the right side of (a), (b) and (c). Scale bar is 1 nm. (d) In-plane and out-of-plane spacings between planes as seen along [110] of LSMO in the HZO twin variant shown in (c). The distance between consecutive La_{2/3}Sr_{1/3}O planes is around $3.9 \pm 0.1 \text{ \AA}$, and that between plane x and 1 is around $2.3 \pm 0.1 \text{ \AA}$.

We observe rather striking features at the uppermost plane of the LSMO electrode (denoted with an “x” and marked with a yellow arrow in Figures 1a, b and c) and at the lowermost plane of the HZO layer. The intensity in a Z-contrast image is approximately proportional to the squared atomic number (Z^2) of the columns. Hence, the heavier cation columns appear brighter than the lighter cation columns. The anion columns (oxygen) are not visible due to the limited dynamic range of the detector. Accordingly, the Z-contrast images shown in Figure 1 give the expected contrast of an AMO_3 perovskite, such as the LSMO. The most intense atomic columns correspond to the mixed La/Sr ($Z_{La} = 57$, $Z_{Sr} = 38$) sublattice, whereas Mn ($Z_{Mn} = 25$) atomic columns appear slightly dimmer. While this holds true for both [100] and [110] zone axes, the uppermost plane with LSMO structure (denoted as “x”) shows a more intense atomic column than expected. Had the LSMO buffer layer ended with a MnO_2 plane, its intensity would have been lower. This is clearly evidenced by tracing the profile intensity across the interface and comparing the intensity of the atomic plane x in both images, which is much higher than expected from the MnO_2 planes. Indeed, it suggests that Mn has been substituted by a much heavier atom, even heavier than La. Strikingly, the intensity of the first atomic plane of the HZO structure, named i in Figure 1, is lower than expected, which implies that the concentration of the heavy Hf ($Z_{Hf} = 72$) and to an extent, Zr ($Z_{Zr} = 40$), is lower in this plane.

Further insights into this interface can be extracted by analyzing the spacings across the interface. For that, Gaussian curves were fitted to each atomic column in the observation plane of Figure 1c. Then, the distances between the centers of first neighbor Gaussians are taken as in-plane and out-of-plane spacings and the averaged values are plotted as a function of the out-of-plane position, as shown in Figure 1d (see a complete 2D mapping of spacings across the interface in Figure S4, Supplemental Material [37]). The results show that the in-plane and out-of-plane spacings are, for both HZO and LSMO layers, constant beyond the interface and coinciding with the expected values, [26] 3.14 and 2.96 Å for HZO in-plane (distance equal to 3/2 of the distance

between [-211] planes) and out-of-plane (111) spacings, respectively, and 2.76 and 3.9 Å for LSMO. Recall that the LSMO layer is fully strained on the STO substrate, thus replicating the in-plane lattice parameters of 3.9 Å for STO. However, the out-of-plane spacings at the interface deviate from the expected ones. Indeed, the distance between planes x and i (the first plane with HZO structure) is larger than the (111) HZO spacing (3.35 Å vs. 2.96 Å), and the planes (half the distance between $La_{2/3}Sr_{1/3}O$ planes), 2.3 Å vs. 1.95 Å, respectively. It is worth noting that the out-of-plane spacings of the HZO twin variant shown in Figure 1b across the interface follow the same trend (spacings profiles not shown here). These results show the presence of a sharp interface between such dissimilar structures, as opposed to the presence of a strain gradient in interfaces involving different perovskites such as $LaAlO_3/SrTiO_3$. [38]

To reveal the chemistry at the interface, we used electron energy loss spectroscopy (EELS) to obtain chemical maps with atomic resolution. Figure 2a shows a Z-contrast image of the interface. Figures 2b, c, d, e and f show elemental maps of La-M, Sr-L, Mn-L, Hf-M and Zr-L edges, respectively, from an EEL spectrum image that was acquired simultaneously with the Z-contrast image. The atomic resolution elemental maps reveal that the last plane that can be considered chemically LSMO is a $La_{0.67}Sr_{0.33}O$ plane. Likewise, different areas within the TEM specimen as well as different TEM specimens were inspected by EELS; they all revealed $La_{0.67}Sr_{0.33}O$ to be the last plane with LSMO chemical composition. However, the termination of the STO substrate is mostly TiO_2 terminated (Figure S5, Supplemental Material [37]) and therefore LSMO is expected to be primarily MnO_2 , with minor areas having $La_{0.67}Sr_{0.33}O$ termination. [27,28]. Hence, the Mn expected to be present at the upper surface of LSMO has been substituted by Hf/Zr atoms, as sketched in Figure 2g, although in the A-terminated areas the Hf/Zr is added as a metal in the B site of the perovskite. In addition, the dimmer intensity of the first atomic plane shown by the Hf and Zr elemental maps suggest a lower concentration of these two elements right at the HZO/LSMO interface. These results account for the contrast observed in planes x

and i of the Z-contrast images shown in Figure 1, and prove that a chemical reconstruction takes place at the HZO/LSMO interface.

Similar features are observed at the m-HZO/LSMO interface, with Hf/Zr occupying the Mn sites in layer x. However, HAADF images and EELS elemental maps of this interface show that the content of La and Hf/Zr in layers 1 and x, respectively, are lower (see Figure S2, Supplemental Material [37]).

ratio is close to that of LSMO compound, with a mix of Mn⁺² and Mn⁺³. [39] But more importantly, the Mn L₂₃ ratio remains unchanged on moving toward the interface, see Figure 3a and b. Hence, Mn does not change its oxidation state when approaching the HZO layer.

Regarding the O-K edge (Figure 3e), it shows a rather abrupt transition at the heterointerface, in agreement with the abrupt structural and chemical

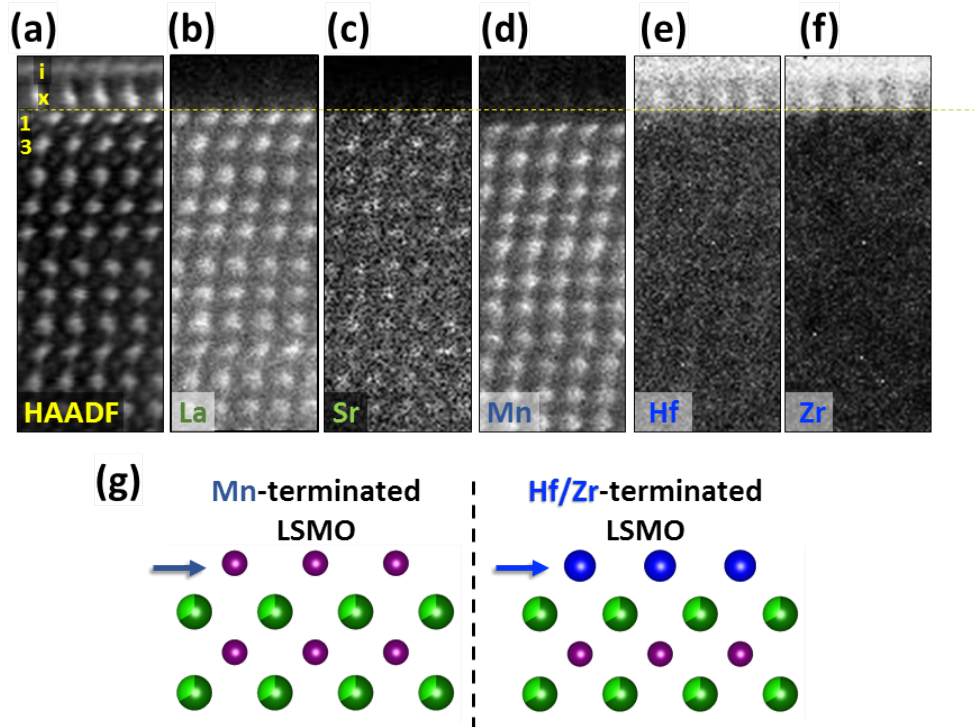


FIG 2. (a) HAADF image acquired simultaneously with the EEL spectrum-image dataset along the [100] zone axis. (b), (c), (d), (e) and (f) elemental maps of La-M, Sr-L, Mn-L, Hf-M and Zr-L edges, respectively. (g) Sketch of the uppermost region of the LSMO layer illustrating the substitution of the terminating Mn plane by Hf/Zr cations. Mn (purple), Hf/Zr (blue), La (dark green) and Sr (light green) atoms are shown.

EELS also allows tracking changes in the electronic structure across the interface. It is well known that Mn-L and O-K edges are sensitive to changes in bonding, coordination and the oxidation state of Mn. [39] Figure 3 shows the Mn-L and O-K edges from spectra acquired plane by plane (Figure 3a and 3e), starting far below the interface till the HZO layer (Figure 3c). The Mn-L edge includes the L₃ and L₂ white lines at onset energies of about 640 and 650 eV, respectively. The intensity ratio of the L₃ and L₂ lines of the Mn L_{2,3} edge (the L₂₃ ratio) correlates with the oxidation state of Mn. [39] The measured Mn L₂₃

variations shown in Figure 1 and 2. Within the LSMO layer, the O-K edge shows a pre-peak, with an energy onset at ~527 eV. The pre-peak disappears after the interface between LSMO and HZO), as shown in Figure 3e. This is not the only change that takes place in the O-K edge pre-peak, as its intensity decreases in the uppermost Mn plane as well; see Figure 3f, where two O-K edge spectra are compared, one from plane 1 and one from the lowermost MnO₂ plane shown (plane 8 in Figure 3c). This pre-peak is sensitive to the partially filled 2p states of oxygen, which are hybridized with 3d states of manganese. Therefore, its

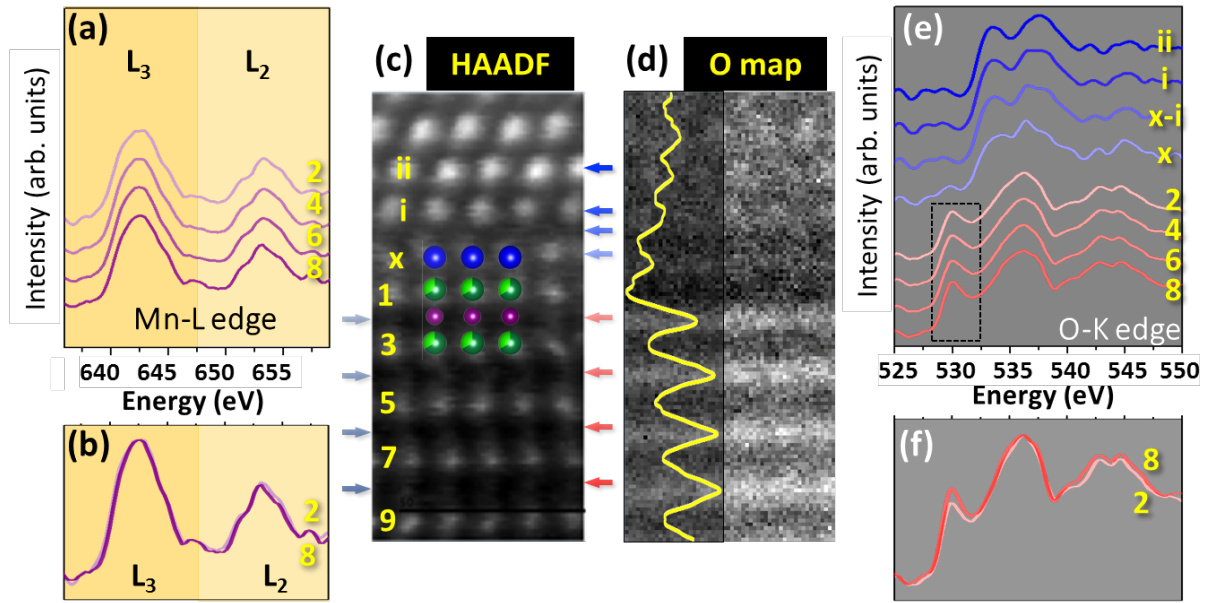


FIG 3. Change of electronic fine structure across the LSMO/o-HZO heterointerface tracked using row-averaged Mn L-edge (a) and O-K edge (e). (b) and (f) superimposed spectra of the uppermost (2) and lowermost (8) MnO₂ planes of Mn-L and O-K edges, respectively. (c) shows the HAADF image (acquired along the [110] LSMO zone axis) from where spectra in (a) and (e) have been extracted, with the cation model structure superimposed (Mn (purple), Hf/Zr (blue), La (dark green) and Sr (light green)). The colors of the spectra (in (a), (b), (e) and (f)) and of the arrows (in (c)) indicate the element analyzed in each atomic plane, with Hf/Zr in blue, O in red and Mn in purple. The intensity ratio of the O pre-peak (at 527 eV) and the main peak (at 535 eV) is ~ 0.3 in the layers further from the interface, while this ratio becomes smaller (~ 0.2) at the interface, as shown in (f). (d) O elemental map across the LSMO/o-HZO heterointerface and the corresponding intensity profile (yellow background) shows a smaller O signal at the interface, indicating that a smaller quantity of O is present. The O map in (d) was obtained by integrating the O-K in each pixel from around 527 eV to around 540 eV.

variation in intensity is signaling either the presence of oxygen vacancies or transfer of electrons from Hf/Zr found in the perovskite plane x, or both; although the EELS oxygen elemental map in Figure 3d reveals a weaker oxygen signal at the interface (especially at plane x), indicating that oxygen is less abundant at the interface (see also Figure S6, Supplemental Material [37]). The evolution of the fine structure as a function of the probe position can be obtained using a combination of DFT calculations and simulations based on dynamical scattering theory. [40,41] However, given the lack of a precise atomic model of the HZO/LSMO interface, such simulations are unfeasible. Yet, our EELS experiments suggest the unambiguous presence of oxygen vacancies based on the total lower signal at the interface and the lower O pre-peak intensity.

From the STEM experiments, we observe that the MnO₂-terminated surface layer of LSMO undergoes a chemical reconstruction; specifically, Mn atoms are substituted by Hf/Zr atoms. The LSMO top surface is expected to exhibit MnO₂ termination, [27,28] provided that the STO is mostly TiO₂ terminated, and the stoichiometry is maintained in films grown by pulsed laser deposition (Figure S5, Supplemental Material [37]). Instead, we find Hf/Zr atoms at the said layer. Moreover, an oxygen deficiency is detected at the interface, which indicates that the substitution of Mn atoms by Hf occurs under oxygen deprivation conditions. The presence of oxygen vacancies at the interface may also be relevant during the ferroelectric switching and screening, [42,43] and electroresistance. [6,44] Interfacial reconstructions leading to the formation of a hybrid atomic plane bridging two dissimilar

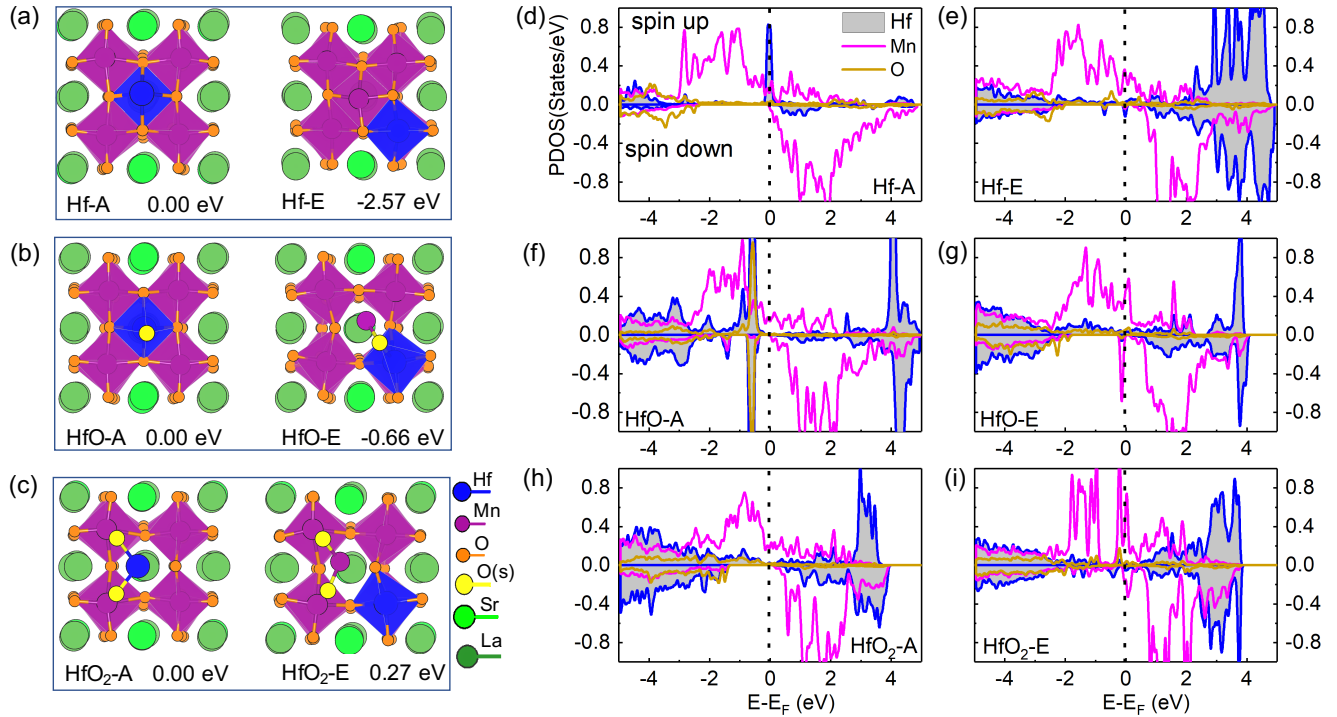


FIG 4. (a-c) Top view of $\text{La}_{0.75}\text{Sr}_{0.25}\text{MnO}_3$ slabs with Hf (Hf-A), HfO (HfO-A) or HfO₂ (HfO₂-A) clusters adsorbing on the MnO_2 -terminated surface, left panel, and the Hf atom exchanging position with a surface Mn atom and getting embedded in the LSMO matrix (Hf-E, HfO-E and HfO₂-E), right panel. The conformations are represented by ball-and-stick models. Oxygen atoms adsorbing on LSMO surface are labeled as O(s). The relative energies with reference to the HfO_x -A configurations are also shown. (d-i) Spin-polarized, atom-projected density of states (PDOS) of surface atoms in Hf-A, Hf-E, HfO-A, HfO-E, HfO₂-A and HfO₂-E configurations.

structures have been reported to allow for heteroepitaxy of dissimilar oxides as binary oxides on perovskites. [45] These results rule out the presence of a tetragonal HZO phase at the LSMO/o-HZO interface of the explored specimen –the two atomic planes under the o-HZO structure contain La/Sr (plane 1) and Hf/Zr (plane x) cations at the perovskite A and M sites, respectively– contrary to what has been previously reported in an equivalent heterostructure. [19] Furthermore, the HZO cation sublattice shows structural features incompatible with the tetragonal phase, see Figure S7 of the Supplemental Material [37]. In brief, Figure S7 shows that both the spacings and angles between atomic columns on the observation plane (corresponding to the (Hf/Zr) cation sublattice) reveal the expected “breathing” (periodic larger and smaller spacings and angles) of the orthorhombic phase,

ruling out the presence of the tetragonal phase at the interface.

The large dissimilarity between the structure of HZO and LSMO results in a complex heterointerface that involves thousands of atoms, [26] and prohibits the simulation of the heterointerface and extract its energy and electronic structure using DFT calculations. Instead, to understand the driving force for Hf substitution at the MnO_2 layer, we have simulated the initial growth process and compared the energetics of HfO_x ($x = 0, 1, 2$) clusters deposited as adatoms on MnO_2 as opposed to Hf substituting Mn. More complex HfO_x clusters ($x > 2$) on MnO_2 surface are beyond the scope of this work due to computational limitations. The adsorption and substitution of Hf, HfO and HfO₂ on MnO_2 are shown using atomic models in Figures 4(a-c), respectively. For classification, the structures with Hf adatom on the surface and Hf substituting Mn at the MnO_2 -

terminated layer are referred to as Hf-A and Hf-E, respectively. The corresponding structures of HfO are labeled as HfO-A and HfO-E, and that of HfO₂ as HfO₂-A and HfO₂-E, respectively. For the adatom clusters, we find that the Hf atom tends to adsorb at the center of four neighboring Mn atoms of the MnO₂ surface. Subsequently, we exchange the positions of the Hf adatom and a Mn atom of the surface to get the Hf-E, HfO-E and HfO₂-E configurations.

For a single Hf atom, we find that the Hf-Mn exchange (Hf-E configuration) lowers the total energy by 2.57 eV from the Hf-A configuration, as shown in Figure 4(a). Therefore, there is a significant thermodynamic driving force for the formation of Hf-E from Hf-A. To understand this substitution, we analyze the electronic structure of the two configurations. The atom-projected density of states of the adatom and the top layer of LSMO for both Hf-A and Hf-E configurations are shown in Figures 4(d, e), respectively. We find that the adsorption of Hf on

tendency for the formation of oxygen vacancy at the MnO₂ surface on adsorption of Hf and the Hf-Mn exchange. The results are shown in Figure S9 (Supplemental Material [37]). The results are consistent with Hf-A and Hf-E without any oxygen vacancies.

The difference in the electronic structure of the Hf-A and Hf-E configurations, and the passivation of the dangling bonds with Hf_{Mn} substitution can be further understood from an analysis of the surface charges based on nominal oxidation states. The nominal oxidation state of Mn in La_{0.67}Sr_{0.33}MnO₃ is +3.33. In bulk, the two oxygen in a Mn^{+3.33}O₂⁻² unit need 4 electrons, and Mn only donates 3.33e, so Mn^{+3.33}O₂⁻² plane has a charge of +0.67 per unit cell. Similarly, the (La_{0.67}⁺³Sr_{0.33}⁺²O⁻²) plane has a net charge of -0.67 per unit cell. Along [001] direction in bulk LSMO, each (La_{0.67}Sr_{0.33}O) plane can be assumed as donating 0.335 e/unit cell to its two adjacent MnO₂ layers. The MnO₂-terminated surface,

Table I. Bader charges analysis of MnO₂-terminated LSMO surface without and with Hf clusters.

Configuration (2×2 MnO ₂)	Bader atomic charge (e)			
	Average surface Mn	Hf	Average surface O	Surface charge
Bare MnO ₂ surface	5.40		7.06	2.08
Hf-A	5.49	2.26	7.11	1.10
Hf-E	5.42	1.81	7.08	0.13
HfO-A	5.45	1.90	7.09	1.51
HfO-E	5.50	1.73	7.08	1.45
HfO ₂ -A	5.38	1.76	7.03	1.58
HfO ₂ -E	5.40	1.75	7.02	1.55

the surface of MnO₂ results in large localized states around the Fermi energy, and these states are primarily derived from the Hf adatom. It indicates that Hf chemisorption induces surface dangling bonds, which leads to the higher energy of the Hf-A configuration. The electronic structure of Hf-E configuration in Figure 4(e) shows that the Hf-Mn exchange leads to a significant reduction of the Hf-states near the Fermi energy due to the passivation of the dangling bonds. We have also analyzed the

therefore, has a charge of +0.335 per unit cell, as it receives 0.335 e/unit cell from only the underlying (La_{0.67}Sr_{0.33}O) layer. There are 4 MnO₂ units in the termination layer of the supercell, hence the total surface charge is +1.34. The preferred oxidation state of Hf is +4. Hence, the substitution of Mn^{+3.33} by Hf⁺⁴ in MnO₂ contributes extra 0.67 e for the entire (2 × 2) MnO₂ layer, reducing the total surface charges from +1.34 to +0.67 for the MnO₂ layer. A Bader charge analysis [46]— that partitions the valence electrons to

atoms using a zero-flux surface where the electron density is minimum — of the two configurations, supports these results. We find that with the substitution of Mn by Hf in Hf-E, the Bader charge of the termination layer greatly reduces to 0.13 e from 1.10 e in Hf-A (**Table I**).

Apart from Hf on top of the MnO₂ layer, we have also analyzed the energetics of HfO and HfO₂ clusters on MnO₂-terminated LSMO (Figure 4 (b-c)). For molecular HfO adsorption, its results are similar to Hf atom with the HfO-E configuration being 0.66 eV lower in energy than the HfO-A configuration. The mechanisms involved are similar to that of Hf atom. HfO chemisorption induces surface dangling bonds in HfO-A and drives its energy higher (Figure 4(f)). Hf-Mn exchange leads to a significant reduction of the Hf-states near the Fermi energy due to passivation of the dangling bonds (Figure 4 (g)), and lowers the energy of the corresponding structure.

The behavior of HfO₂ cluster on MnO₂-terminated LSMO (Figure 4(c)) is different from that of Hf and HfO molecules, with the HfO₂-A configuration being lower in energy by 0.27 eV from the HfO₂-E configuration. The reason for the different behavior of HfO₂ is that the HfO₂ cluster adsorbed on the MnO₂ surface does not have any surface dangling bonds, as observed from the density of states of Hf in Figure 4(h). The exchange between Hf and Mn does not lead to any significant charge rebalance at the surface (Table I). Moreover, in the HfO₂-E configuration, surface Mn-O bonds are partly broken due to the embedding of Hf (See the increase in Mn-O bond lengths in Figure S8, Supplemental Material [37]). These broken bonds induce large localized states near the Fermi energy (Figure 4(i)) and increase the energy of the corresponding structure.

The variation in adsorption energy of Hf, HfO and HfO₂ on LSMO with respect to the oxygen chemical potential are given in Figure S8. It is observed that Hf-E is the most stable configuration when $\mu_{\text{O}} < -6.99$ eV; i.e., under intermediate to Hf-rich (O-poor) growth conditions spanning a large

range of μ_{O} values. For a small range of -6.99 eV $< \mu_{\text{O}} < -6.44$ eV, we find HfO-E to be most stable. When $\mu_{\text{O}} > -6.44$ eV, i.e., under oxygen-rich conditions HfO₂-A becomes the most stable configuration on surface MnO₂. These results showing the stability of Hf-E over a large range of μ_{O} values support the experimentally observed reduction in the EEL signal of the O-K edge at the interface due to formation of oxygen vacancies.

IV. CONCLUSIONS

In conclusion, the chemical and structural features of the HZO/LSMO heterointerface that allows epitaxial growth of ferroelectric HZO on perovskites have been revealed. Atomic resolution HAADF images and elemental maps show the chemical reconstruction of the MnO₂-terminated surface of LSMO occurs during the epitaxial growth of HZO on the LSMO, which is supported by DFT calculations of total energy and electronic structure. The reconstruction consists of the substitution of the Mn cations of the MnO₂ interface with HZO by a mixture of Hf/Zr atoms, with Hf/Zr occupying the sites of the Mn in the LSMO perovskite. Such a reconstruction occurs under oxygen deprivation conditions. These results are a critical step towards understanding the decisive role of the LSMO buffer in the stabilization of the ferroelectric phase in thin films of (Hf,Zr)O₂. It is expected to encourage further studies owing to the critical role the interface plays on both the stabilization of the ferroelectric phase and its switching.

ACKNOWLEDGEMENTS

Financial support from the Spanish Ministry of Science, Innovation and Universities, through the “Severo Ochoa” Programme for Centres of Excellence in R&D (SEV-2015-0496) and MAT2017-85232-R (AEI/FEDER, EU) and PID2019-107727RB-I00 (MINECO/FEDER, EU) projects, and from Generalitat de Catalunya (2017 SGR 1377) is acknowledged. SE acknowledges the Spanish Ministry of Economy, Competitiveness and

Universities for his PhD contract (SEV-2015-0496-16-3) and its cofunding by the ESF. SE work has been done as a part of his Ph.D. program in Materials Science at Universitat Autònoma de Barcelona. The electron microscopy performed at ORNL was supported by the Materials Sciences and Engineering Division of Basic Energy Sciences of the Office of Science of the U.S. Department of Energy. The work at Washington University was supported by the National Science Foundations (NSF) through grant numbers DMR-1931610 (T.C.) and DMR-1806147 (R.M.). This work used the computational resources of the Extreme Science and Engineering Discovery Environment (XSEDE), which is supported by NSF ACI-1548562.

- [1] H.J. Lee, M. Lee, K. Lee, J. Jo, H. Yang, Y. Kim, S. C. Chae, U. Waghmare, and J. H. Lee, *Scale-Free Ferroelectricity Induced by Flat Phonon Bands in HfO₂*, *Science* **369**, 1343 (2020).
- [2] S. S. Cheema, D. Kwon, N. Shanker, R. dos Reis, S. L. Hsu, J. Xiao, H. Zhang, R. Wagner, A. Datar, M. R. McCarter, C. R. Serrao, A. K. Yadav, G. Karbasian, C. H. Hsu, A. J. Tan, L. C. Wang, V. Thakare, X. Zhang, A. Mehta, E. Karapetrova, R. V. Chopdekar, P. Shafer, E. Arenholz, C. Hu, R. Proksch, R. Ramesh, J. Ciston, and S. Salahuddin, *Enhanced Ferroelectricity in Ultrathin Films Grown Directly on Silicon*, *Nature* **580**, 478 (2020).
- [3] J. Junquera and P. Ghosez, *Critical Thickness for Ferroelectricity in Perovskite Ultrathin Films*, *Nature* **422**, 506 (2003).
- [4] T. S. Böske, J. Müller, D. Bräuhaus, U. Schröder, and U. Böttger, *Ferroelectricity in Hafnium Oxide Thin Films*, *Appl. Phys. Lett.* **99**, 102903 (2011).
- [5] Y. Wei, S. Matzen, T. Maroutian, G. Agnus, M. Salverda, P. Nukala, Q. Chen, J. Ye, P. Lecoeur, and B. Noheda, *Magnetic Tunnel Junctions Based on Ferroelectric Hf_{0.5}Zr_{0.5}O₂ Tunnel Barriers*, *Phys. Rev. Appl.* **12**, 031001 (2019).
- [6] M. C. Sulzbach, S. Estandía, X. Long, J. Lyu, N. Dix, J. Gàzquez, M. F. Chisholm, F. Sánchez, I. Fina, and J. Fontcuberta, *Unraveling Ferroelectric Polarization and Ionic Contributions to Electroresistance in Epitaxial Hf_{0.5}Zr_{0.5}O₂ Tunnel Junctions*, *Adv. Electron. Mater.* **6**, 1900852 (2020).
- [7] M. C. Sulzbach, S. Estandía, J. Gàzquez, F. Sánchez, I. Fina, and J. Fontcuberta, *Blocking of Conducting Channels Widens Window for Ferroelectric Resistive Switching in Interface-Engineered Hf_{0.5}Zr_{0.5}O₂ Tunnel Devices*, *Adv. Funct. Mater.* **30**, 2002638 (2020).

- [8] E. Yurchuk, J. Müller, R. Hoffmann, J. Paul, D. Martin, R. Boschke, T. Schlösser, S. Müller, S. Slesazeck, R. Van Bentum, M. Trentzsch, U. Schröder, and T. Mikolajick, *HfO₂-Based Ferroelectric Field-Effect Transistors with 260 Nm Channel Length and Long Data Retention*, in *2012 4th IEEE International Memory Workshop, IMW 2012* (2012).
- [9] M. H. Park, Y. H. Lee, T. Mikolajick, U. Schroeder, and C. S. Hwang, *Review and Perspective on Ferroelectric HfO₂-Based Thin Films for Memory Applications*, *MRS Commun.* **8**, 795 (2018).
- [10] M. H. Park, Y. H. Lee, H. J. Kim, Y. J. Kim, T. Moon, K. Do Kim, J. Müller, A. Kersch, U. Schroeder, T. Mikolajick, and C. S. Hwang, *Ferroelectricity and Antiferroelectricity of Doped Thin HfO₂-Based Films*, *Adv. Mater.* **27**, 1811 (2015).
- [11] J. Müller, U. Schröder, T. S. Böske, I. Müller, U. Böttger, L. Wilde, J. Sundqvist, M. Lemberger, P. Kücher, T. Mikolajick, and L. Frey, *Ferroelectricity in Yttrium-Doped Hafnium Oxide*, *J. Appl. Phys.* **110**, 114113 (2011).
- [12] J. Muller, T. S. Boscke, S. Muller, E. Yurchuk, P. Polakowski, J. Paul, D. Martin, T. Schenk, K. Khullar, A. Kersch, W. Weinreich, S. Riedel, K. Seidel, A. Kumar, T. M. Arruda, S. V. Kalinin, T. Schlosser, R. Boschke, R. Van Bentum, U. Schroeder, and T. Mikolajick, *Ferroelectric Hafnium Oxide: A CMOS-Compatible and Highly Scalable Approach to Future Ferroelectric Memories*, in *Technical Digest - International Electron Devices Meeting, IEDM* (2013), pp. 10.8.1-10.8.4.
- [13] J. Müller, T. S. Böske, U. Schröder, S. Mueller, D. Bräuhäus, U. Böttger, L. Frey, and T. Mikolajick, *Ferroelectricity in Simple Binary ZrO₂ and HfO₂*, *Nano Lett.* **12**, 4318 (2012).
- [14] T. Shimizu, K. Katayama, T. Kiguchi, A. Akama, T. J. Konno, and H. Funakubo, *Growth of Epitaxial Orthorhombic YO_{1.5}-Substituted HfO₂ Thin Film*, *Appl. Phys. Lett.* **107**, 032910 (2015).
- [15] K. Katayama, T. Shimizu, O. Sakata, T. Shiraishi, S. Nakamura, T. Kiguchi, A. Akama, T. J. Konno, H. Uchida, and H. Funakubo, *Orientation Control and Domain Structure Analysis of {100}-Oriented Epitaxial Ferroelectric Orthorhombic HfO₂-Based Thin Films*, *J. Appl. Phys.* **119**, 134101 (2016).
- [16] T. Li, N. Zhang, Z. Sun, C. Xie, M. Ye, S. Mazumdar, L. Shu, Y. Wang, D. Wang, L. Chen, S. Ke, and H. Huang, *Epitaxial Ferroelectric Hf_{0.5}Zr_{0.5}O₂ Thin Film on a Buffered YSZ Substrate through Interface Reaction*, *J. Mater. Chem. C* **6**, 9224 (2018).

- [17] J. Lyu, I. Fina, J. Fontcuberta, and F. Sánchez, *Epitaxial Integration on Si(001) of Ferroelectric Hf_{0.5}Zr_{0.5}O₂ Capacitors with High Retention and Endurance*, ACS Appl. Mater. Interfaces **11**, 6224 (2019).
- [18] Z. Zhang, S. L. Hsu, V. A. Stoica, H. Paik, E. Parsonnet, A. Qualls, J. Wang, L. Xie, M. Kumari, S. Das, Z. Leng, M. McBriarty, R. Proksch, A. Gruverman, D. G. Schlom, L. Q. Chen, S. Salahuddin, L. W. Martin, and R. Ramesh, *Epitaxial Ferroelectric Hf_{0.5}Zr_{0.5}O₂ with Metallic Pyrochlore Oxide Electrodes*, Adv. Mater. **33**, 2006089 (2021).
- [19] Y. Wei, P. Nukala, M. Salverda, S. Matzen, H. J. Zhao, J. Momand, A. S. Everhardt, G. Agnus, G. R. Blake, P. Lecoeur, B. J. Kooi, J. Íñiguez, B. Dkhil, and B. Noheda, *A Rhombohedral Ferroelectric Phase in Epitaxially Strained Hf_{0.5}Zr_{0.5}O₂ Thin Films*, Nat. Mater. **17**, 1095 (2018).
- [20] J. Lyu, I. Fina, R. Solanas, J. Fontcuberta, and F. Sánchez, *Robust Ferroelectricity in Epitaxial Hf_{1/2}Zr_{1/2}O₂ Thin Films*, Appl. Phys. Lett. **113**, 082902 (2018).
- [21] H. Y. Yoong, H. Wu, J. Zhao, H. Wang, R. Guo, J. Xiao, B. Zhang, P. Yang, S. J. Pennycook, N. Deng, X. Yan, and J. Chen, *Epitaxial Ferroelectric Hf_{0.5}Zr_{0.5}O₂ Thin Films and Their Implementations in Memristors for Brain-Inspired Computing*, Adv. Funct. Mater. **28**, 1806037 (2018).
- [22] S. Estandía, N. Dix, J. Gazquez, I. Fina, J. Lyu, M. F. Chisholm, J. Fontcuberta, and F. Sánchez, *Engineering Ferroelectric Hf_{0.5}Zr_{0.5}O₂ Thin Films by Epitaxial Stress*, ACS Appl. Electron. Mater. **1**, 1449 (2019).
- [23] S. Estandía, J. Gazquez, M. Varela, N. Dix, M. Qian, R. Solanas, I. Fina, and F. Sanchez, *Critical Effect of Bottom Electrode on Ferroelectricity of Epitaxial Hf_{0.5}Zr_{0.5}O₂ Thin Films*, J. Mater. Chem. C **9**, 3486 (2021).
- [24] T. Li, M. Ye, Z. Sun, N. Zhang, W. Zhang, S. Inguva, C. Xie, L. Chen, Y. Wang, S. Ke, and H. Huang, *Origin of Ferroelectricity in Epitaxial Si-Doped HfO₂ Films*, ACS Appl. Mater. Interfaces **11**, 4139 (2019).
- [25] X. Sang, E. D. Grimley, T. Schenk, U. Schroeder, and J. M. Lebeau, *On the Structural Origins of Ferroelectricity in HfO₂ Thin Films*, Appl. Phys. Lett. **106**, 162905 (2015).
- [26] S. Estandía, N. Dix, M. F. Chisholm, I. Fina, and F. Sánchez, *Domain-Matching Epitaxy of Ferroelectric Hf_{0.5}Zr_{0.5}O₂(111) on La_{2/3}Sr_{1/3}MnO₃(001)*, Cryst. Growth Des. **20**, 3801 (2020).

- [27] F. Sánchez, C. Ocal, and J. Fontcuberta, *Tailored Surfaces of Perovskite Oxide Substrates for Conducted Growth of Thin Films*, Chem. Soc. Rev. **43**, 2272 (2014).
- [28] P. Yu, W. Luo, D. Yi, J. X. Zhang, M. D. Rossell, C. H. Yang, L. You, G. Singh-Bhalla, S. Y. Yang, Q. He, Q. M. Ramasse, R. Erni, L. W. Martin, Y. H. Chu, S. T. Pantelides, S. J. Pennycook, and R. Ramesh, *Interface Control of Bulk Ferroelectric Polarization*, Proc. Natl. Acad. Sci. U. S. A. **109**, 9710 (2012).
- [29] R. Meyer, R. Waser, K. Prume, T. Schmitz, and S. Tiedke, *Dynamic Leakage Current Compensation in Ferroelectric Thin-Film Capacitor Structures*, Appl. Phys. Lett. **86**, 142907 (2005).
- [30] I. Fina, L. Fábrega, E. Langenberg, X. Mart, F. Sánchez, M. Varela, and J. Fontcuberta, *Nonferroelectric Contributions to the Hysteresis Cycles in Manganite Thin Films: A Comparative Study of Measurement Techniques*, J. Appl. Phys. **109**, 074105 (2011).
- [31] G. Kresse and J. Furthmüller, *Efficient Iterative Schemes for Ab Initio Total-Energy Calculations Using a Plane-Wave Basis Set*, Phys. Rev. B - Condens. Matter Mater. Phys. **54**, 11169 (1996).
- [32] P. E. Blöchl, *Projector Augmented-Wave Method*, Phys. Rev. B **50**, 17953 (1994).
- [33] J. P. Perdew, K. Burke, and M. Ernzerhof, *Generalized Gradient Approximation Made Simple*, Phys. Rev. Lett. **77**, 3865 (1996).
- [34] H. J. Monkhorst and J. D. Pack, *Special Points for Brillouin-Zone Integrations*, Phys. Rev. B **13**, 5188 (1976).
- [35] H. Chen and S. Ismail-Beigi, *Ferroelectric Control of Magnetization in $La_{1-x}Sr_xMnO_3$ Manganites: A First-Principles Study*, Phys. Rev. B - Condens. Matter Mater. Phys. **86**, 024433 (2012).
- [36] A. M. Glazer, *The Classification of Tilted Octahedra in Perovskites*, Acta Crystallogr. Sect. B Struct. Crystallogr. Cryst. Chem. **28**, 3384 (1972).
- [37] See Supplemental Material at [URL Will Be Inserted by Publisher] for Complementary Figures and Information.
- [38] J. Gazquez, M. Stengel, R. Mishra, M. Scigaj, M. Varela, M. A. Roldan, J. Fontcuberta, F. Sánchez, and G. Herranz, *Competition between Polar and Nonpolar Lattice Distortions in Oxide Quantum Wells: New Critical Thickness at Polar Interfaces*, Phys. Rev. Lett. **119**, 106102 (2017).

- [39] M. Varela, M. P. Oxley, W. Luo, J. Tao, M. Watanabe, A. R. Lupini, S. T. Pantelides, and S. J. Pennycook, *Atomic-Resolution Imaging of Oxidation States in Manganites*, Phys. Rev. B - Condens. Matter Mater. Phys. **79**, 085117 (2009).
- [40] M. P. Prange, M. P. Oxley, M. Varela, S. J. Pennycook, and S. T. Pantelides, *Simulation of Spatially Resolved Electron Energy Loss Near-Edge Structure for Scanning Transmission Electron Microscopy*, Phys. Rev. Lett. **109**, 246101 (2012).
- [41] B. D. Forbes, A. J. D'Alfonso, R. E. A. Williams, R. Srinivasan, H. L. Fraser, D. W. McComb, B. Freitag, D. O. Klenov, and L. J. Allen, *Contribution of Thermally Scattered Electrons to Atomic Resolution Elemental Maps*, Phys. Rev. B - Condens. Matter Mater. Phys. **86**, 024108 (2012).
- [42] P. Nukala, M. Ahmadi, Y. Wei, S. de Graaf, S. Matzen, H. W. Zandbergen, B. Kooi, and B. Noheda, *Operando Observation of Reversible Oxygen Migration and Phase Transitions in Ferroelectric Devices*, **arXiv:2010**, Submitted: 21 Oct 2020 (2020).
- [43] Y. M. Kim, A. Morozovska, E. Eliseev, M. P. Oxley, R. Mishra, S. M. Selbach, T. Grande, S. T. Pantelides, S. V. Kalinin, and A. Y. Borisevich, *Direct Observation of Ferroelectric Field Effect and Vacancy-Controlled Screening at the BiFeO₃/La_xSr_{1-x}MnO₃ Interface*, Nat. Mater. **13**, 1019 (2014).
- [44] C. Ferreyra, M. Rengifo, M. J. Sánchez, A. S. Everhardt, B. Noheda, and D. Rubi, *Key Role of Oxygen-Vacancy Electromigration in the Memristive Response of Ferroelectric Devices*, Phys. Rev. Appl. **arXiv:2006**, Submitted:18 Jun 2020. (2020).
- [45] X. Gao, S. Lee, J. Nichols, T. L. Meyer, T. Z. Ward, M. F. Chisholm, and H. N. Lee, *Nanoscale Selfflating for Oxide Epitaxy with Large Symmetry Mismatch*, Sci. Rep. **6**, 38168 (2016).
- [46] W. Tang, E. Sanville, and G. Henkelman, *A Grid-Based Bader Analysis Algorithm without Lattice Bias*, J. Phys. Condens. Matter **21**, 084204 (2009).
- [47] Tao, L. L.; Paudel, T. R.; Kovalev, A. A.; Tsybal, E. Y. Reversible Spin Texture in Ferroelectric HfO₂. *Phys. Rev. B* **2017**, *95*, 245141.
- [48] U. Schroeder, C. Richter, M. H. Park, T. Schenk, M. Pešić, M. Hoffmann, F. P. G. Fengler, D. Pohl, B. Rellinghaus, C. Zhou, C. C. Chung, J. L. Jones, and T. Mikolajick, *Lanthanum-Doped Hafnium Oxide: A Robust Ferroelectric Material*, Inorg. Chem. **57**, 2752 (2018).

